Supporting Information

Identify the Activity Origin of Pt Single-atom CATALYST via Atom-by-Atom Counting

Shuhui Liu,[†,#] Hua Xu,[‡,#] Dongdong Liu,[§] Hao Yu,[‡] Fan Zhang,[§] Peng zhang[‡], Ruolin Zhang,[‡] Wei Liu*[,§]

[†] Dalian Jiaotong University, Dalian, 794 Huanghe Road, Liaoning 116028, China

[‡] Petrochemical Research Institute, China National Petroleum Corporation, 100007 Beijing, China

[§] Division of Energy Research Resources, Dalian National Laboratory for Clean Energy, Dalian Institute of Chemical Physics, Chinese Academy of Sciences, 457 Zhongshan Road, Dalian, Liaoning 116023, China

Corresponding Author

Wei Liu –Dalian National Laboratory for Clean Energy, Dalian Institute of Chemical Physics, Chinese Academy of Sciences, 457 Zhongshan Road, Dalian, Liaoning 116023, China;
E-mail: weiliu@dicp.ac.cn
ORCID: https://orcid.org/0000-0002-4403-737X

Table of Contents for the Supplementary Information:

1. EMARS Methodology

1.1 Flowchart of EMARS

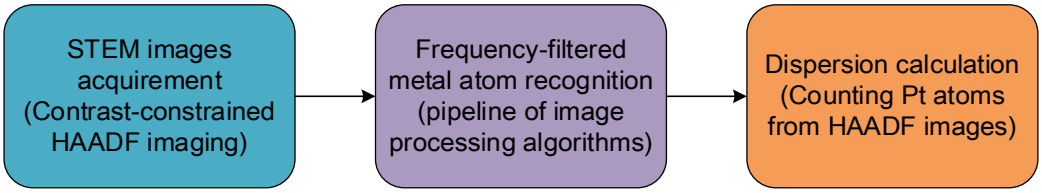

Figure S1. Flowchart of EMARS strategy principally divided into three steps, including STEM images acquirement, frequency-filtered metal atom recognition, and dispersion calculation.

1.2 STEM images acquirement

Since a structure statistic method should emphasizes more on the output reliability in order to provide the objective evaluation on the atom dispersion. Comparability among HAADF images has to be ensured for minimizing influence of image contrast deviation[1-2]. Therefore, the HAADF imaging condition setup was adopted to guarantee uniform contrast standard regarding on scattering strengths from Pt species, which to our knowledge would benefit the solution of atoms counting via a 3D tomography in the future progress[3-4]. Specifically, imaging parameters have been kept consistent for imaging process, including ones forming the electron probe as well as signal transition settings for both DF-detector and STEM imaging controller. For the STEM sample preparation, the Pt/Al_2O_3 catalysts before and after reaction were dispersed in ethanol, dropped onto the copper grids and dried on a hot plate (100 ^{o}C). The atomic resolution microscopy analysis, including the static HAADF imaging for EMARS as well as the identical location STEM microscopy study were performed on a JEM ARM200F thermal-field emission microscope with a probe *Cs*-corrector working at 200 kV. Parameter details about the experimental setup are provided in the session of experimental details.

1.3 Frequency-filtered metal atoms/clusters recognition

The algorithm principle of EMARS method

For a manual counting approach on a HAADF image, the contrast interference from oxide support leads to the major loss of atom recognition. Limited by the human visual capability on HAADF image contrast, it induces remarkable loss of metal atoms supported at thick regions during statistics. With advantage of quantitative calculation, information at thick regions of catalyst is able to be extracted using EMARS method since the contrast deviation at these locations is still numerically enough owned to the large scattering difference between a noble metal atom (Pt) and the oxide supports (Al_2O_3). In addition, the EMARS method allows us to selectively remove contrast interference of the Al_2O_3 support to sharpen the intuitive contrast of Pt species and further promote the atom recognition precision.

The metal atom/particle identification pipeline

The metal atom/particle identification pipeline is presented in **Figure S2**, consisting of top hat operation, frequency domain transformation, image sharpening, dynamic threshold binarization. The original image of the supported metal catalyst is displayed in **Figure S2a**. The metal atoms/clusters are in brightest-contrast, the substrate is in lower brightness, and the background is in dark contrast. In order to count the distribution of metal atoms/clusters dispersion, it requires to recognize the bright contrast in the image, including individual Pt atoms, clusters. **Figure S2b** illustrates the result after white top hat transformation. The top hat transform (**Equation S1**), a method of image morphology defined as the image subtracting the result of the image opening ($\circ$) operation,[5] can highlight bright areas in a darker background.

$$\boldsymbol{T_{hat}(f) = f - (f \circ b)} \qquad \text{(Equation S1)}$$

To identify the metal atoms/clusters, the substrate needs to be removed. Since the contrast of Al_2O_3 substrate concentrates in the low frequency range, while for metal atoms/clusters that are as small as several pixels in HAADF image, the contrast mainly locates at the high frequency domain. Benefiting for such characteristic, Al_2O_3 support and Pt metal species can be primarily distinguished within contrast frequency range. Specifically, a high-pass filter was used to filter out the low frequency to eliminate the substrate after the Fast Fourier Transform (FFT) transformation (**Figure S2c**), and then an inverse FFT transformation was performed to yield the contrast-selectively-promoted image (**Figure S2d**). It can be seen that the contrast from the Al_2O_3 support have been compressed to low level, while the residual background was further removed with applying a Laplace kernel filter[5] that further improved the recognition accuracy. As shown **in Figure S2e**, the promoted contrast between metal atoms, oxide supports, and image background offers foundation in high quality for the following metal atom recognition.

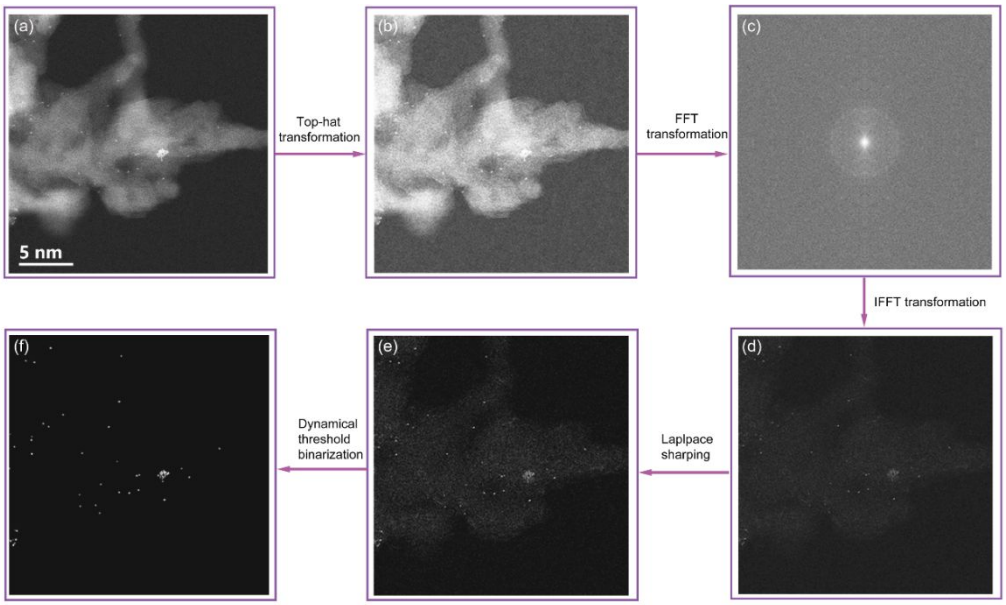

Figure S2. Pipeline of atom identification in EMARS architecture, all the images share the same scale bar of 5nm.

Dynamically threshold method for binarization

To automatically binarize the massive images output from Laplace sharpening, a dynamically threshold method is developed. Firstly, histogram statistics were performed on a large number of images output from Laplace sharpening, as revealed in **Figure S3a**, where the gray values were normalized. The histograms of the HAADF images do not demonstrate two-peak or multi-peaks phenomenon, but only an individual peak, which induces difficulty to select a threshold by the traditionally method of determining valley bottom. It is therefore a dynamically threshold method was used for image binarization. The image contains three parts and the binarization threshold needs to be selected between the gray support and the bright metal atoms. Therefore, the black background needs to be removed firstly. Through the normalized histogram, it can be inferred that the background accounts for about 50% of the histogram. Therefore, the low value was assigned as the pixel intensity in the 50% of the histogram, and the high value was selected as the one in the 99% of the histogram. The binarization threshold $\boldsymbol{T_i}$ is obtained by the **Equation S2** iteratively,

$$\boldsymbol{T_{i+1}} = \frac{\mathbf{1}}{\mathbf{2}}\left(\frac{\sum_{k=low}^{T_i} \boldsymbol{h_k} \times \boldsymbol{k}}{\sum_{k=low}^{T_i} \boldsymbol{h_k}} + \frac{\sum_{k=T_i+1}^{high} \boldsymbol{h_k} \times \boldsymbol{k}}{\sum_{k=T_i+1}^{high} \boldsymbol{h_k}}\right) \qquad \text{(Equation S2)}$$

where $\boldsymbol{h_k}$ is the proportion of pixels when the gray value is k, and iterative calculation is performed until $|\boldsymbol{T_{i+1}} - \boldsymbol{T_i}| < \boldsymbol{\Delta}$.

General idea of the dynamic threshold binarization method

The general idea of the dynamic threshold method is explained as in **Figure S3b**. The threshold value was used to divide the grayscale data, and the input image was divided into foreground and background pixel by pixel. The foreground integrator and background integrator were used to get the averaged value, and then a new threshold value was obtained. Repeating this process until the threshold change becomes small, the final segmentation results of atom identification were achieved, as depicted in **Figure S2f**. More results are shown in **Figure S4**.

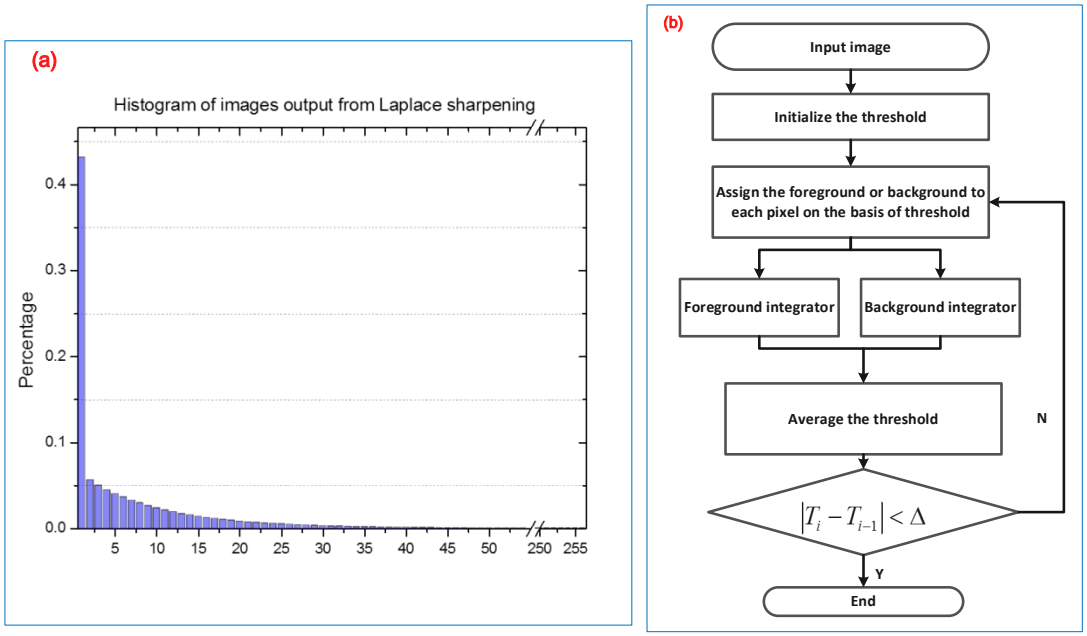

Figure S3. Illustration of dynamic threshold method (a) Histogram of images output from Laplace sharpening; (b) Flowcharts of the dynamic threshold method

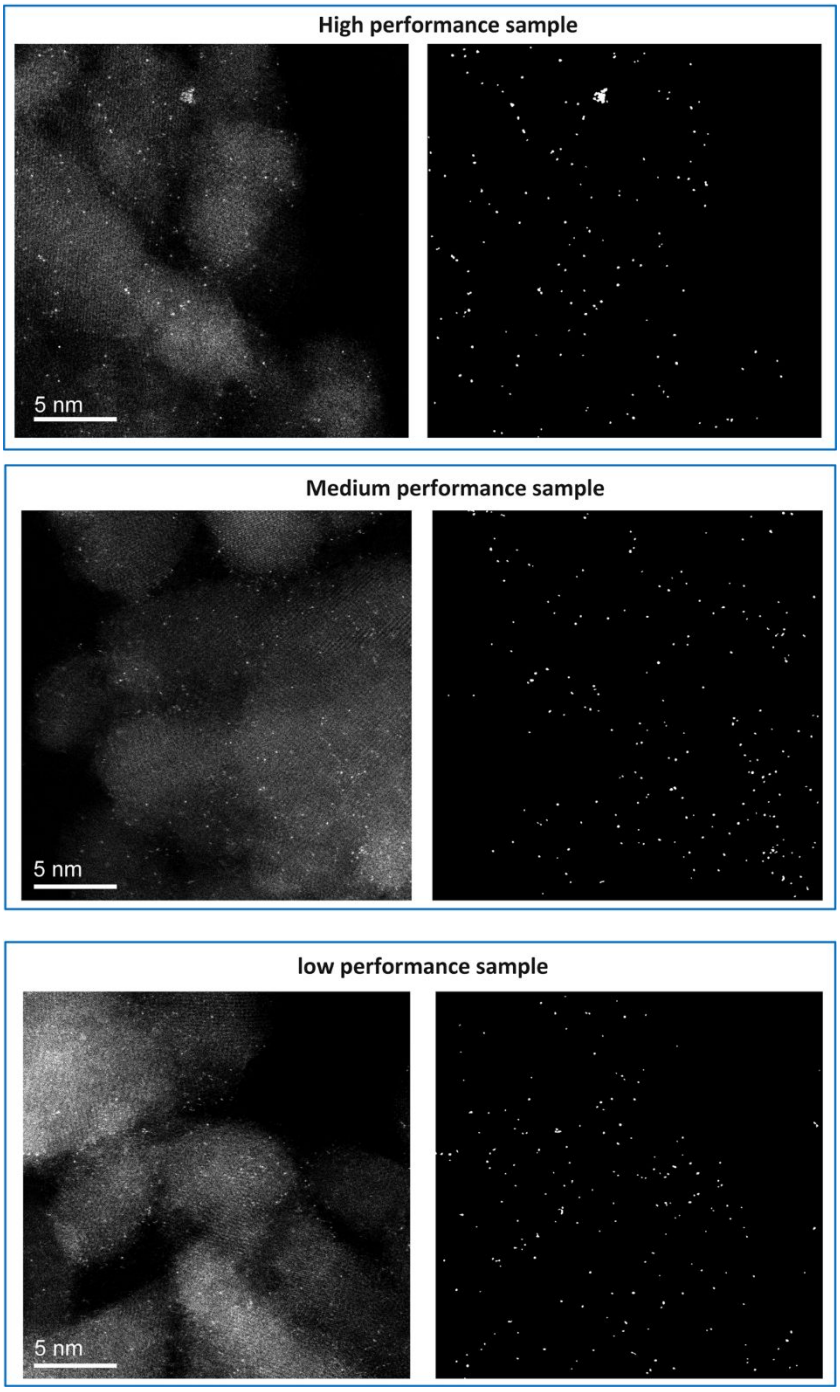

Figure S4. Visualization of Pt atom identification results for samples with high, medium, and low catalytic activity of aromatics production, respectively.

1.4 Dispersion Calculation Using Precise Atom Coordinates

Separation of the catalyst region from blank background

The success of atom identification enables us to collect accurate coordinates of all Pt species, including both single atoms and clusters, on which catalyst dispersion could be redefined and quantitatively estimated via utilizing specially developed scripting. In addition, since a HAADF image normally contains blank background besides the catalyst regions, the blank area has to be identified and excluded from calculating the efficient sample area so as to yield an accurate Pt dispersion density. This treatment was implemented by a script composed of Gaussian filter, binarization, and morphological processing. In the result of processed HAADF image, **Figure 2f** highlights the identified boundary that presents well separation of the catalyst region from blank background.

Calculation method of single atoms in a Pt cluster

As one primary form of Pt atoms, contribution from Pt clusters to the metal dispersion as well as catalytic activity are of high significance to be evaluated since traditional knowledge believes Pt cluster plays important role on catalysis activity. Specifically, a strategy of single atom normalization was utilized to quantify potential influence of Pt clusters. Since the imaging and recognition process is consistent for both single atom and cluster, the number of single atoms contained in a Pt cluster could be calculated by **Equation S3**,

$$\boldsymbol{N_i^j} = \frac{\boldsymbol{S_{ci}^j}}{\frac{1}{\boldsymbol{N_i^{atom}}}\sum_{\boldsymbol{m=1}}^{\boldsymbol{N_i^{atom}}} \boldsymbol{S_{si}^m}} \qquad \text{(Equation S3)}$$

where $\boldsymbol{N_i^j}$ is the atoms number contained in the cluster j from image i, $\boldsymbol{S_{ci}^j}$is the projected area of cluster j in HAADF image i, $\boldsymbol{S_{si}^m}$ is equivalent area of the Pt single atom m in image i, $\boldsymbol{N_i^{atom}}$is the total number of Pt single atoms in image *i*.

2. Dispersion Results

Atom identification and statistics based on EMARS

On the foundation of precise Pt identification via EMARS, the dispersion is redefined as the Pt atoms density derived from two descriptions, the single Pt atoms and single&cluster ones, so as to explore the contribution from different Pt coordinating species. It should be noticed that Pt nanoparticles were not considered for dispersion evaluation because there were almost no particles identified for the three catalysts in constant Pt loading as low as 0.28 w.t.%, making particles are in ignorable contribution to the reforming activity. **Table S1** presents the result of atom identification and statistics based on EMARS.

Catalysis Performance and dispersions from different methods

As shown in **Table S3**, the activity values of the MP and LP samples by EMARS method were normalized relative to that of HP one. Following the same way, results for reforming activity (**Table S2**) and HOT (**Table S4**) were both normalized using the HP sample as the benchmark. Specifically, **Table S2** utilizes the yields of aromatics from petroleum reforming products to represent efficient catalytic activity. The higher the aromatic content, the higher activity the reforming catalyst has, the more alkanes and cycloalkanes in the raw material transformed into aromatic products.

Table S1. EMARS Results of Pt/Al_2O_3 Catalysts with Different Activity

Sample category	Total HAADF images	Total Pt single atoms	Total sample area ($nm^2 \cdot Al_2O_3$)	Atoms density of single Pt (Pt_1/nm^2)	Total atoms contained in Pt clusters	Atoms density of single&cluster Pt (Pt_{1+c}/nm^2)
High performance ($HP\text{-}Pt/Al_2O_3$)	158	18879	45982	0.4106	2971	0.4752
Medium performance ($MP\text{-}Pt/Al_2O_3$)	138	16135	42397	0.3806	306	0.3878
Low performance ($LP\text{-}Pt/Al_2O_3$)	125	14051	40713	0.3451	121	0.3481

Table S2. Catalysis Performance of Pt/Al_2O_3 Catalysts Evaluated via Aromatic Yields

Sample category	Reaction Temp/°C	Aromatics Yields/wt%	Normalized Activity
HP-Pt/Al_2O_3	490	70.8	100%
MP-Pt/Al_2O_3		63.7	90.0%
LP-Pt/Al_2O_3		58.9	83.2%

Table S3. Pt Atoms Dispersion Evaluated via EMARS Method

Sample category	Dispersion of Single Pt Atoms (EMARS-Pt_1)		Dispersion of Single&Cluster Pt Atoms (EMARS-Pt_{1+c})	
	Measured Density (Pt_1/nm^2)	Normalized Density	Measured Density (Pt/nm^2)	Normalized Density
HP-Pt/Al_2O_3	0.4106	100%	0.4752	100%
MP-Pt/Al_2O_3	0.3806	92.7%	0.3878	81.6%
LP-Pt/Al_2O_3	0.3451	84.0%	0.3481	73.2%

Table S4. Pt Atoms Dispersion Evaluated via HOT Method

Sample category	Measured Dispersion	Normalized Dispersion
HP-Pt/Al_2O_3	95.7%	100%
MP-Pt/Al_2O_3	69.9%	73.1%
LP-Pt/Al_2O_3	50.0%	52.2%

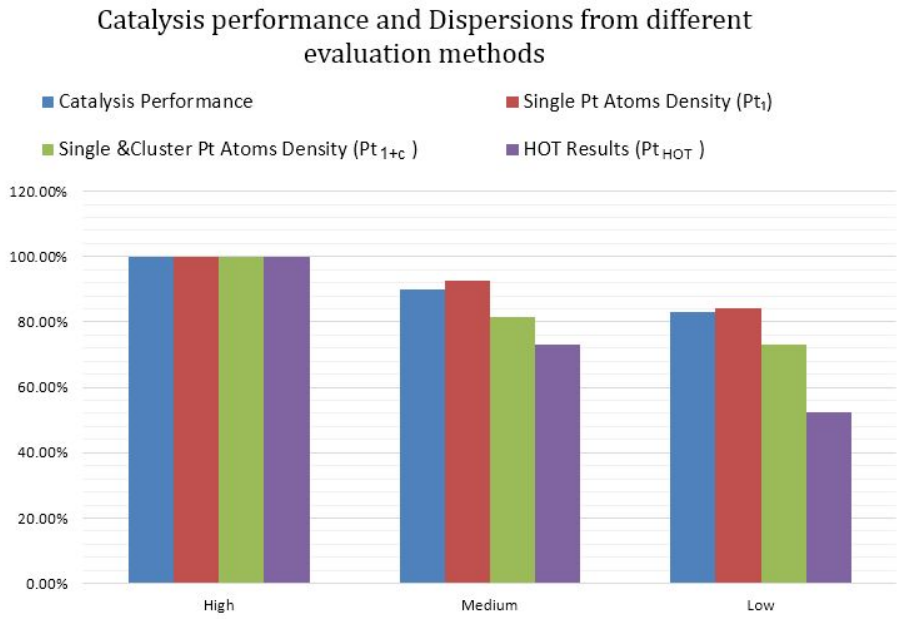

Figure S5. Correlation diagram about catalysis activities and Pt atom dispersions through EMARS and HOT evaluations, where high-performance data was used as reference. All the data were normalized using data of high-performance sample as the reference.

Correlation calculation between actual activity and the integrated contribution of Pt_1 atoms

To make comprehensive comparison on the performances of HOT and EMARS, activities of Pt/Al_2O_3 catalysts have been referred to evaluate the accuracy of two methods. **Figure S5** illustrates the normalized activities as well as Pt dispersions derived from data of **Tables S1~S4**. It unambitiously demonstrates that the EMARS strategy in this work provides Pt dispersion evaluation at precision remarkably better than that of HOT. This novel method rooting from atom-resolved microscopy would provide more quantitative information distinct from traditional statistics, e.g. Pt-Pt distances distribution $n_i(D)$ ($i = H,M,L$), correlation of metal distance and activity *Y(T)*, Pt atoms coordination in clusters et al., thereby offers opportunity to directly identify catalytically active species via fractional analysis.

$$\mathrm{Y}(T) = \left(\frac{N_H(T)}{N_M(T)} - \frac{P_H}{P_M}\right)^2 + \left(\frac{N_H(T)}{N_L(T)} - \frac{P_H}{P_L}\right)^2 + \left(\frac{N_M(T)}{N_L(T)} - \frac{P_M}{P_L}\right)^2 \qquad \text{(Equation S4)}$$

where $N_H(T) = \int_T^{60Å} n_H(D)\mathrm{d}D_{Pt-Pt}$, $N_M(T) = \int_T^{60Å} n_M(D)\mathrm{d}D_{Pt-Pt}$, $N_L(T) = \int_T^{60Å} n_L(D)\mathrm{d}D_{Pt-Pt}$ obtain the integrated atom numbers with Pt-Pt distance larger than the threshold T for the HP, MP and LP samples, respectively; P_H, P_M, P_L represent the normalized catalytic performance. Y is a function of T representing the correlation relationship between actual activity and the integrated contribution of Pt_1 atoms at distance larger than T. The smaller Y(T) is, the higher consistency it correlates with the catalytic performance. As this curve reaches the smallest deviation at ~3.8Å, it indicates that Pt_1 atoms in distances large than 3.8Å would serve as functional sites to contribute to aromatic producing activity (defined as effective single atoms), whereas the rest of Pt atoms of either P_1, cluster or particle are too close to each other to contribute to producing aromatics during reforming.

3. Reforming Reaction Evaluation Unit

For the catalysis evaluation, a straight-tube fixed-bed in maximum capacity of 100mL was designed to perform the reforming reaction as in Figure S6.

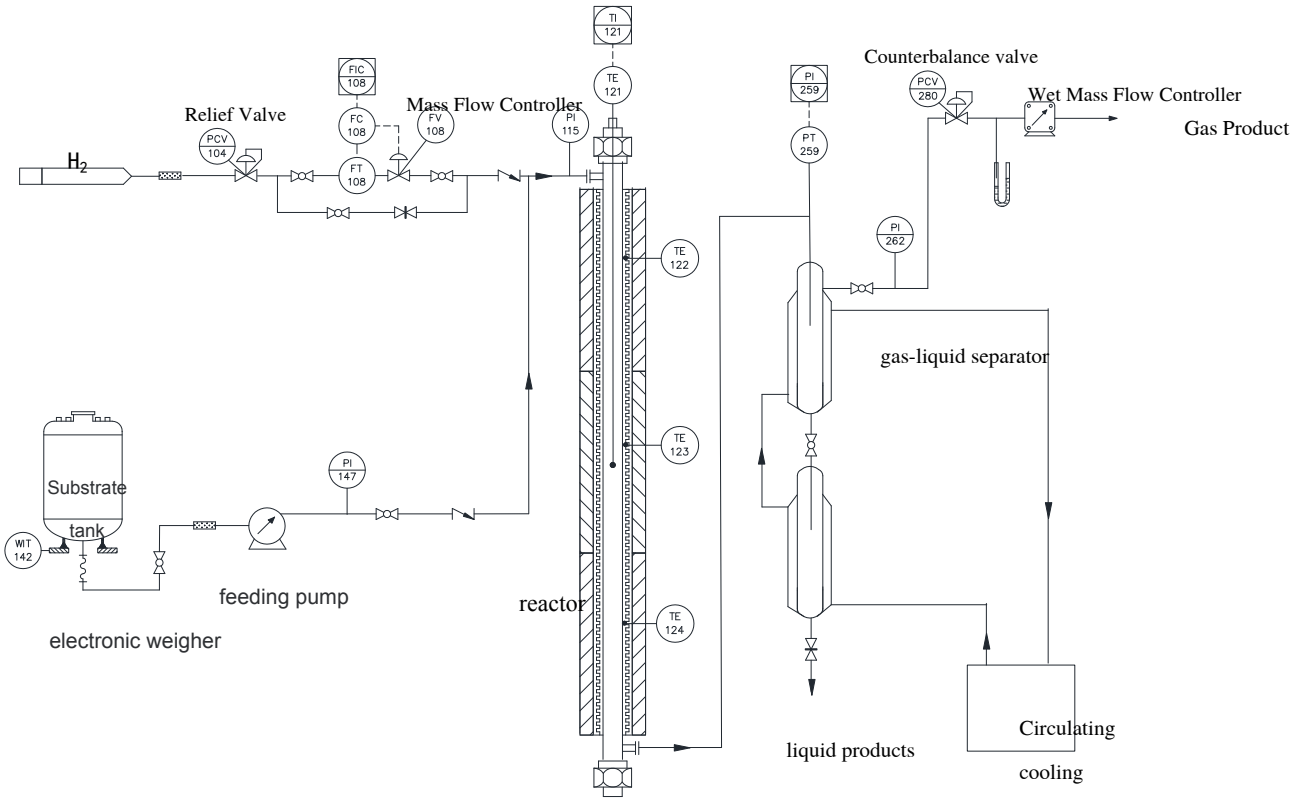

Figure S6. The Flowchart of Fixed-bed Evaluation Unit for Catalytic Reforming

References

(1) Krivanek, O. L.; Chisholm, M. F.; Nicolosi, V.; Pennycook, T. J.; Corbin, G. J.; Dellby, N.; Murfitt, M. F.; Own, C. S.; Szilagyi, Z. S.; Oxley, M. P.; Pantelides, S. T.; Pennycook, S. J. Atom-by-atom structural and chemical analysis by annular dark-field electron microscopy. *Nature* **2010,** *464*, 571-574.

(2) Pennycook, S. J.; Jesson, D. E. ATOMIC RESOLUTION Z-CONTRAST IMAGING OF INTERFACES. *Acta Metall. Mater.* **1992,** *40*, S149-S159.

(3) Tian, X. Z.; Kim, D. S.; Yang, S. Z.; Ciccarino, C. J.; Gong, Y. J.; Yang, Y.; Yang, Y.; Duschatko, B.; Yuan, Y. K.; Ajayan, P. M.; Idrobo, J. C.; Narang, P.; Miao, J. W. Correlating the three-dimensional atomic defects and electronic properties of two-dimensional transition metal dichalcogenides. *Nat. Mater.* **2020,** *19*, 867-873.

(4) Zhou, J. H.; Yang, Y. S.; Yang, Y.; Kim, D. S.; Yuan, A.; Tian, X. Z.; Ophus, C.; Sun, F.; Schmid, A. K.; Nathanson, M.; Heinz, H.; An, Q.; Zeng, H.; Ercius, P.; Miao, J. W. Observing crystal nucleation in four dimensions using atomic electron tomography. *Nature* **2019,** *570*, 500-503.

(5) Davies, E. R., *Computer and Machine Vision: Theory, Algorithms, Practicalities*. 4th ed.; ELSEVIER: 2012; p 912.